processes

MDPI

*Article*

# Investigation on Water Invasion Mode and Remaining Oil Utilization Rules of Fractured-Vuggy Reservoirs: A Case Study of the Intersection Region of S99 Unit in Tahe Oilfield

**Hong Cheng, Feiyu Yuan *, Shiliang Zhang, Lu Li, Xianping Luo and Bo Chen**

No.2 Oil Production Plant, SINOPEC Northwest Company, Korla 841000, China; chenghong.xbsj@sinopec.com (H.C.)
* Correspondence: 18502815749@163.com

**Abstract:** Fractured-vuggy reservoirs are a new target in carbonate oil and gas exploration and development. Because of well-developed reservoir bodies, including fractures and caverns, bottom water invasion can be observed in oilfield development, with low utilization efficiency of crude oil in the reservoir. Accordingly, this study focused on the intersection region of the S99 unit of the Tahe fractured-vuggy reservoirs. Based on seismic data, the reservoir bodies can be divided into three types—caverns, fractures, and broken solution pores. Using the same location condition assignment algorithm, four single-type models are fused into a multi-scale discrete three-dimensional geological model of fractured and cavernous reservoirs, and the corresponding fractured-vuggy reservoir model was established for numerical simulation. The single-well historical fitting precision exceeded 85%. Furthermore, the development can be divided into four stages—initial stage of production, peak production stage, liquid control and oil stabilization stage, and scale gas injection stable. Streamlining sweep analysis determined the utilization and distribution characteristics of the remaining oil in the reservoir. It can be concluded that structure, caverns, and fractures were the main controlling factors affecting the remaining oil distribution in the fractured-vuggy reservoir. The fluid exchange among single-well reserve zones was calculated using streamline-based quantitative sweep analysis and interwell flow quantitative analysis method. Through source-sink quantitative analysis, interwell flow relations were derived, and three water breakthrough modes were further concluded: violent flooding, slow ascending of water cut, and low cut or intermittent water production.

**Keywords:** fractured-vuggy reservoir; numerical simulation; water invasion; streamline sweep; source-sink quantitative analysis; water breakthrough mode



**Citation:** Cheng, H.; Yuan, F.; Zhang, S.; Li, L.; Luo, X.; Chen, B. Investigation on Water Invasion Mode and Remaining Oil Utilization Rules of Fractured-Vuggy Reservoirs: A Case Study of the Intersection Region of S99 Unit in Tahe Oilfield. *Processes* **2023**, *11*, 1833. https://doi.org/10.3390/pr11061833

Academic Editors: Chao Zhang, Fansheng Huang and Tengfei Wang

Received: 3 March 2023
Revised: 13 May 2023
Accepted: 22 May 2023
Published: 16 June 2023



## 1. Introduction

Oil and gas resources in carbonate reservoirs occupy approximately 70% of the global reserves and 50% of the proved recoverable reserves. Oil and gas production exceeds 60% of the global output [1–4]. All of these suggest an essential role of carbonate reservoirs in oil and gas exploration. Compared with conventional sandstone porous medium reservoirs, fluid flow in carbonate reservoirs depend heavily on fractures, with extreme anisotropy [5–8]. Accordingly, carbonate reservoirs differ significantly from conventional sandstone reservoirs in the oil-displacement mechanism, oil well water breakthrough rules [9–12], and the distribution characteristics of remaining oil [13–15]. Fracture and cavern development is the critical factor determining fractured-vuggy carbonate reservoir development [16]. The carbonate rocks in Western China are prolific in oil and gas resources, among which the fractured-vuggy carbonate rocks account for approximately 2/3 of total reserves [17]. The Tahe Oilfield, located at the axis of Akekule uplift, Tarim Basin, is a typical fractured-vuggy carbonate reservoir with 9.35 × 108 t of oil and gas reserves [18]. The Tahe Oilfield is mainly composed of Ordovician carbonate fractured-vuggy reservoirs, with oil and gas resources mainly accumulated in caverns and fractures of different sizes [13,19]. The reservoir bodies have different types and

significant differences in fracture and cavern sizes. They show random distribution patterns and significant anisotropy. The space is effective for oil and gas storage and as the main seepage channel.

With deeper oilfield development, the oil-water interface can gradually increase, and bottom waters gradually create cones of depression, leading to a continuously high water cut in oilfields. However, the remaining oil at the lateral side and the top of oil wells is shielded and can hardly be used [20]. According to previous dynamic monitoring and numerical simulation results, excessive oil remains around and between wells that cannot be effectively controlled and utilized after immiscible nitrogen displacement. Consequently, gaining an in-depth understanding of the distribution pattern of remaining oil in fractured-vuggy reservoirs, strengthening the comprehensive government of reservoirs and exploiting the potential of the remaining oil is of great practical significance to improving the development performance.

Scholars have conducted a great deal of research on the distribution rules of the remaining oil in fractured-vuggy reservoirs. By considering core, logging, seismic data, and production performance, Zheng et al. [13,21] analyzed the multi-scale characteristics and types of reservoir bodies, spatial forms of the distribution pattern of fractures and caverns on the distribution of remaining oil in fractured-vuggy carbonate reservoirs. They concluded four main-controlling factors of the remaining oil distribution after water flooding—local high point, insufficient well control, connected channel mask, and weak hydrodynamic force. Wang et al. [22–24] employed CT scanning and 3D printing technology to establish a 3D visual model of fractured-vuggy reservoirs and performed injection/anti-injection experiments. They proposed a formation mechanism of remaining oil in fractured-vuggy reservoirs under water flooding, mainly including insufficient injection/production well control, difference of gravity between oil and water, interference among flow channels, weakly-connected channel isolation, and weak hydrodynamics forced at the far end. Accordingly, seven remaining oil underwater flooding types are classified: imperfect injection-production patterns, blind-ends, top-attics, streaming under gravity flooding, secondary flow channels, weak channel isolation, and far-end weak connection.

Yang et al. [25] focused on the remaining oil in the TK440 well owned by the Tahe Oilfield. Based on a detailed depiction of fracture-vug structures, a comprehensive analysis of production dynamics and waterlogged characteristics, four distribution patterns of the remaining oil in the Guanhe reservoir were summarized—unused remaining oil in the shallow Anhe River, the remaining oil in the high-level well of deep Anhe River, oil in the attic of the well circumference, and remaining oil at the dark end of Anhe River. Tang et al. [26–28] analyzed the connectivity of carbonate fractured-vuggy reservoirs in the Tahe, the injection-production performance, and the distribution of oil water. Based on actual drilling, measured wells, and injection-production performance, they concluded that the distribution of remaining oil was subjected to geological characteristics of reservoirs, the development characteristics of fracture-vug structures, and the development factors at macroscopic, microscopic, and apparent levels, respectively.

Bottom water lifting is a primary factor that restricts enhancing recovery efficiency. Each year, the decline of production induced by the bottom (up to 10 kt) water lifting is approximately 10% of the reduction. The oil wells in the Tahe fractured-vuggy carbonate reservoirs show complex and diverse water breakthrough rules. However, the subsurface fluid flow rules are still unclear [29,30]. Gaining bottom water invasion mode and rules is significant in inhibiting the optimization and improvement of bottom water technology, enhancing the match between technology and reservoirs, and satisfying oilfield development.

According to the statistics of the production performance of Tahe oil wells, the Tahe carbonate oil wells have different water breakthrough rules from sandstone reservoirs [31–33]. Uniform laws can hardly be derived because of complex and changeable fractured-vuggy media. Based on production fluid data of the No. 29 well in the S48 fractured-vuggy unit, Zhang et al. [34] quantitatively divided water breakthrough characteristics into three types—slow ascending, violent flooding, and transition. Based on the data of the oil wells

in the Yingmai 32-7 plot in the Talimu Oilfield, Xu et al. [35,36] divided water breakthrough into slow ascending, benched ascending, and rapid ascending. Cheng et al. [37–39] analyzed 51 breakthrough wells in Ordovician fractured-vuggy oil and gas reservoirs of the mid-east Tahe and concluded that the water breakthrough ascension could be divided into stable, benched, and violent flooding. Based on three-division schemes, Chen et al. [40,41] expanded the division of water breakthrough in fractured-vuggy carbonate oil wells into slow ascending, benched ascending, rapid ascending, fluctuation, and violent flooding. Scholars clarified water production mechanisms from multiple angles for various water breakthroughs in Tahe Oilfield. Utilizing numerical simulation, Chang et al. [42] investigated the variation characteristics of moisture content in oil wells under different fracture/vug combinations. They analyzed the relations of the number, height, and length of the steps in moisture content curves and the length of the water-free oil production period with fracture/vug combination modes [43,44].

The S99 unit in the Tahe Oilfield is a typical fractured-vuggy carbonate reservoir and has experienced natural energy, injection development, and gas injection development phases. The recovery degree and comprehensive water cut are 13.6% and 23%, respectively. At the early production stage, the well was an expansion-type reservoir and then entered into the long-term elastic water-driven stage, during which bottom water served as driving energy. Therefore, rapid water breakthroughs and waterlogging are common problems in oil well development.

This study focuses on the S99 unit in the Tahe Oilfield, establishing the fine-scale geological model. Numerical simulations were performed on the distribution characteristics of the remaining oil in reservoirs at different development phases. The main controlling factors of the remaining oil distribution were analyzed with streamline sweep conditions to further explore bottom water invasion rules and conclude water invasion mode. This study can provide technical support for the high-efficiency utilization of fractured-vuggy carbonate reservoirs.

## 2. Geological Modeling of S99 Unit Reservoir

### *2.1. Geological Reservoir Profile*

The S99 unit is located in the northern part of the No.10 region. It is a broken-solution reservoir formed under compression and twist of two deep fractures, with well-developed caverns and fractures. The reservoir is abundant in oil and gas resources. From 2018 to 2019, rapid water breakthrough occurred in several high-productivity wells in the S99 unit, and production dropped rapidly. Afterwards, water production can be effectively controlled by adopting reasonable fluid control and injection-production pattern measures. At the later stage of the development, after the implementation of the large-scale gas drive, the composite water content can be controlled within 20%; the current recovery degree of the S99 unit was approximately 13.6%.

The reservoir shows the following characteristics of the northern fracture in the S99 unit: strong continuity of solution caves in static depiction region, scattered distribution of reservoir bodies featured by larger tops and smaller bottoms, interconnection of reservoir bodies via fractures and crushed dissolution pores, and high connectivity among wells that have been validated by interference well test.

### *2.2. Geological Modeling*

The geological model of the intersection area in the S99 unit was constructed based on seismic data. Because of different properties, the reservoir bodies can be classified into caverns, broken solution pores and fractures. Caverns were extracted with wave impedance properties and mainly include core cavern, non-core caverns, and solution holes. The broken solution pores were extracted by tensor attribute while fractures were extracted by ant body attributes. By using deterministic modeling methods, establish discrete large-scale karst cave models and discrete large-scale crack models; Then, under the constraints of karst facies control, based on the probability volume of karst cave development and the probability volume of inter well fracture development, a random modeling multi-attribute

collaborative simulation method is used to establish a karst cave model and a small-scale discrete fracture model. Using the same location condition assignment algorithm, four single-type models are fused into a multi-scale discrete three-dimensional geological model of fractured and cavernous reservoirs, and the corresponding fractured-vuggy reservoir model was established for numerical simulation. The seismic weight was sampled to the geological model using the phase model. Figure 1 displays the engraving figure of the seismic bodies in the intersection area of the S99 unit.

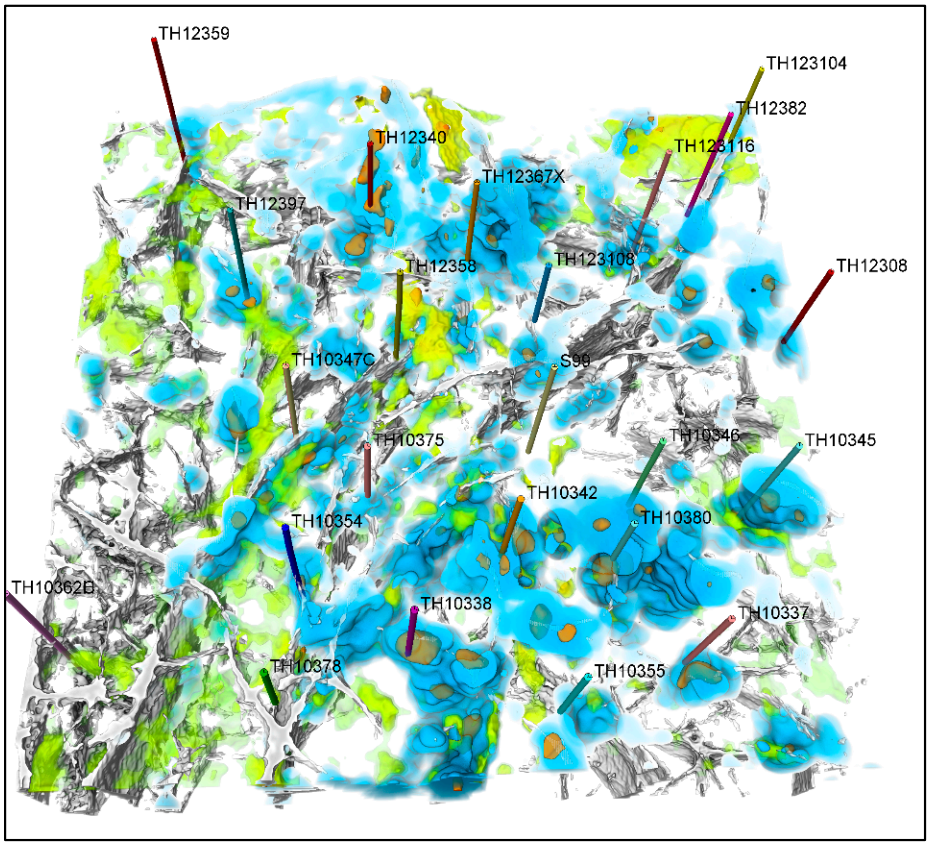


**Figure 1.** Engraving figure of the intersection region of S99 unit.

The geological parameters of the reservoir were further determined. First, the porosity was measured and corrected based on static and dynamic reserve data. Then, by considering the convergence of numerical simulation, the porosity model was smoothed by $4 \times 0.5$ times. Results show that the porosity degrees of core and non-core caverns were 19% and 3.8%, respectively. For the modified model, the geological reserves were 18.59 million tons, with an error of 2.3%. Figure 2 displays the abundance graph of original reserves in the intersection region.

In addition, the permeability showed high uncertainty. Different types of reservoir bodies were assigned with different values. Specifically, the permeabilities of core caverns, non-core caverns, and fractures were 2000 mD, 800 mD, and 60 mD, respectively. Figure 3 displays the permeability distribution pattern in the intersection region of the S99 unit.

The fluid characteristics in the reservoir were determined as listed below. Under in-situ reservoir conditions, the density, the bulk coefficient, and the viscosity of crude oil were 0.9032 g/cm$^3$, 1.0782, and 22.75 mPa·s, respectively. Figure 4 displays the phase diagram of fluid.

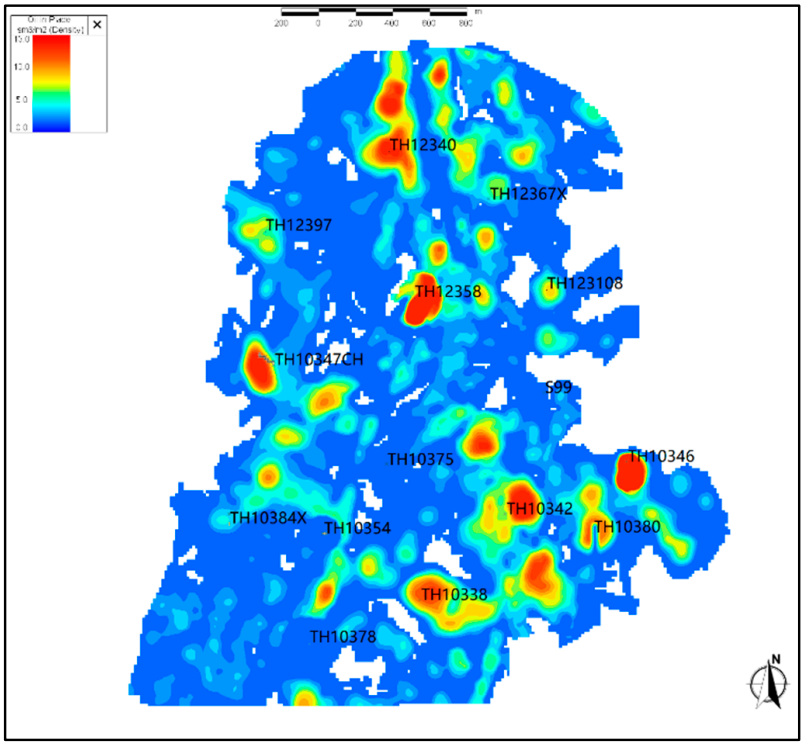


**Figure 2.** Abundance graph of original reserves in the intersection region of S99 unit.

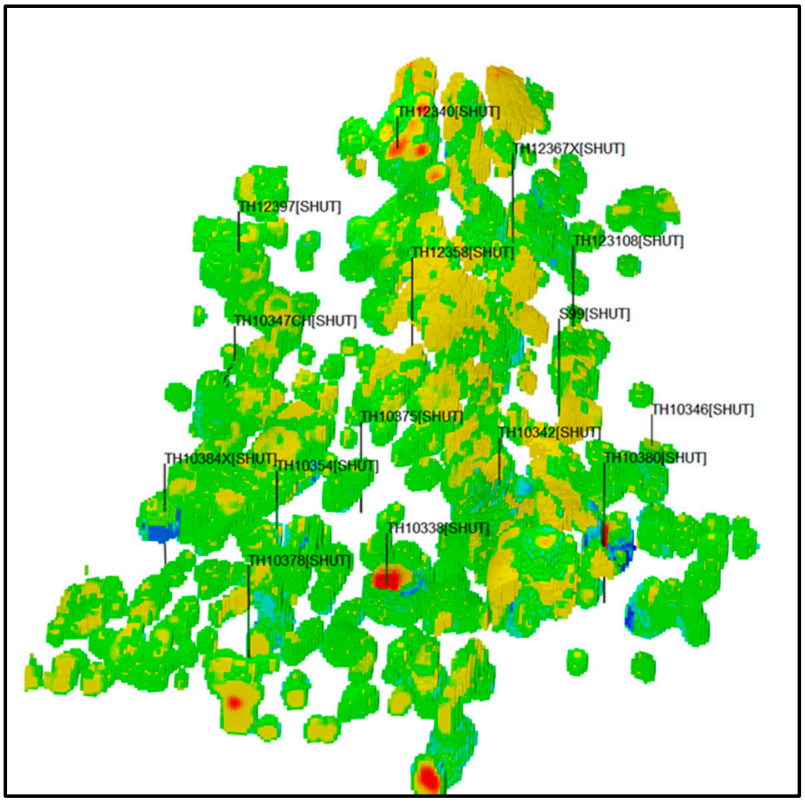


**Figure 3.** Distribution mode of the cave permeability in the intersection region.

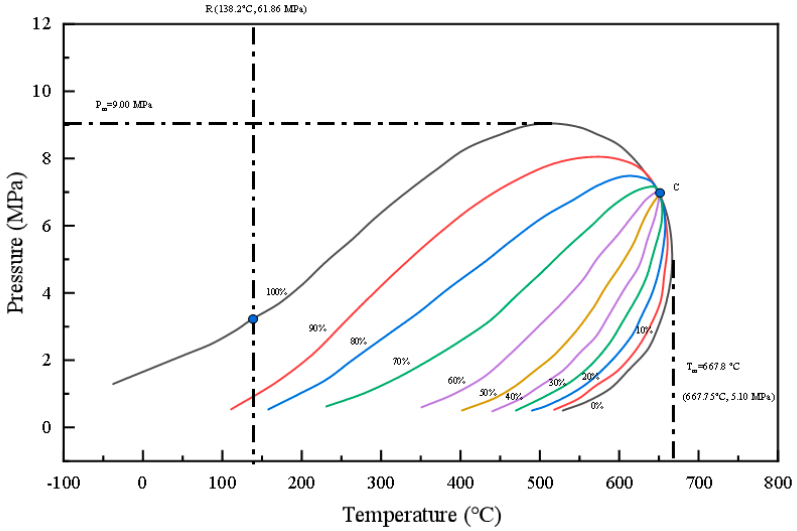


**Figure 4.** Phase diagram of hydrocarbon fluid in the reservoir.

### *2.3. History Fitting*

Because of the high uncertainty of fractured-vuggy reservoir parameters, the reservoir parameters should be reflected with dynamic response characteristics via many iterations and fitting. After the division, 255 × 254 × 100 meshes with the same size of 15 × 15 × 5 m were generated. The total number of meshes was 6,477,000. After 56 iterations in two rounds on the established model of the intersection region of the S99 unit, the overall fitting ratios of regional production, single-well production, and flowing bottomhole pressure (FBHP) were approximately 85%, as shown in Figure 5.

It should be noted that the initial model shows a series of problems, including rapid pressure drop and the short water-cone breakthrough period during a historic fitting in the whole region. This is because the plane permeability in the initial model was low, leading to rapid pressure drop and fast bottom water coning. Based on the reservoir forming process of broken solution, the plane permeability increased gradually from the deep to the shallow reservoir, i.e., the fluid in the shallow reservoir showed strong plane fluidity, and the fluid in the deep reservoir showed strong vertical fluidity. Therefore, the established geological model was adjusted, and the plane permeability was increased by 1~30 times. After the modification, the overall pressure drop of the plot dropped, suggesting abundant water energy. The water magnification was adjusted to 98 times, and the pressure fitting was improved.

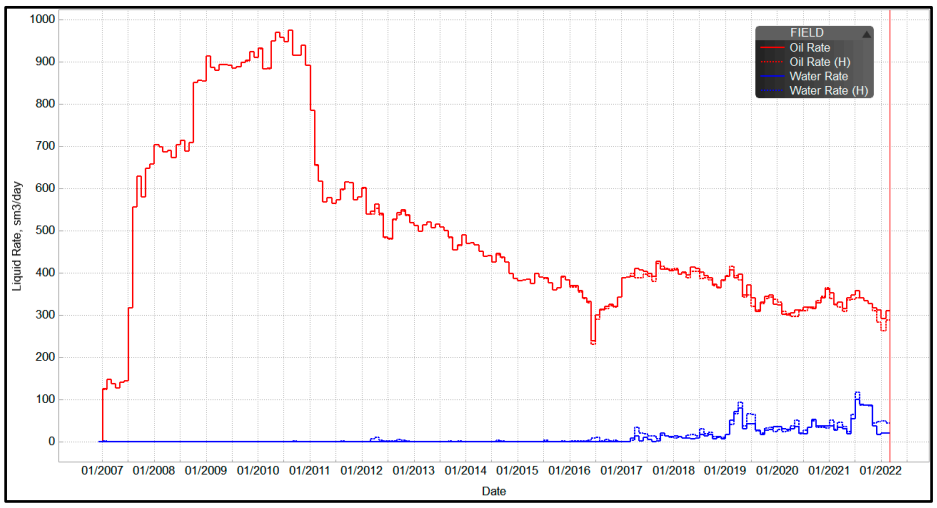


(**a**)

**Figure 5.** *Cont.*

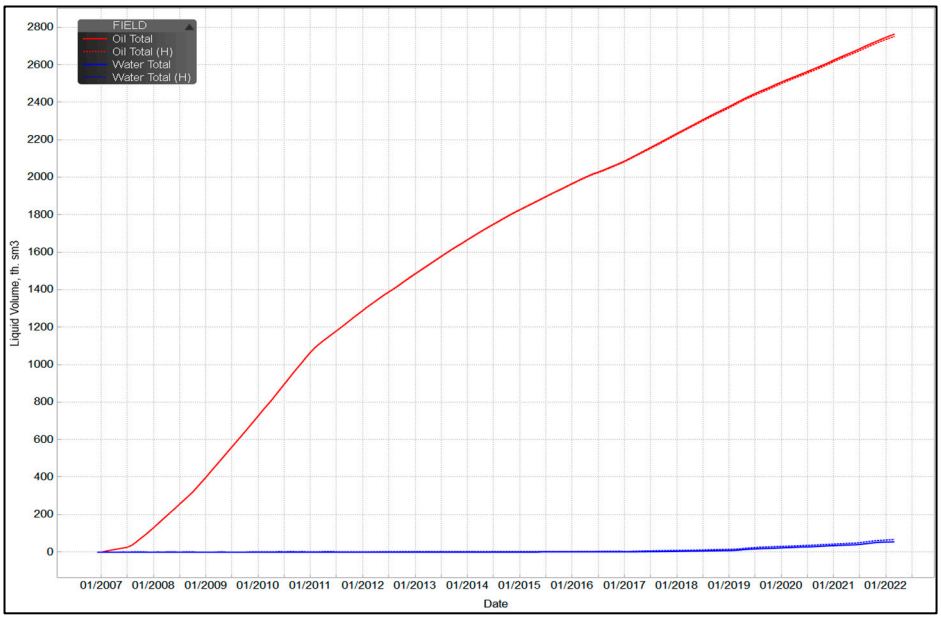


(**b**)

**Figure 5.** Fitting curves of daily (**a**) and cumulative oil/water production (**b**).

Historical fitting was also performed on single-well production, during which the main fitting indexes were daily oil and water production and FBHP. According to the fitting results, the fitting ratios of single-well productions of 15 wells all exceeded 85%, with favorable fitting performance. Therefore, the established geological model was suitable for investigating the remaining oil distribution and the rules of bottom water invasion.

## 3. Distribution Characteristics of Remaining Oil at Different Development Stages and the Related Main Controlling Factors

### *3.1. Division of Development Stages*

The development of the S99 unit was divided into four stages (initial stage of production, peak stage of production, liquid control and oil stabilization stage, and scale gas injection stage) in accordance with production scale and development mode to examine the distribution characteristics of the remaining oil in the reservoir. Figure 6 displays the daily oil (water) productions and daily gas injections at the above four development stages.

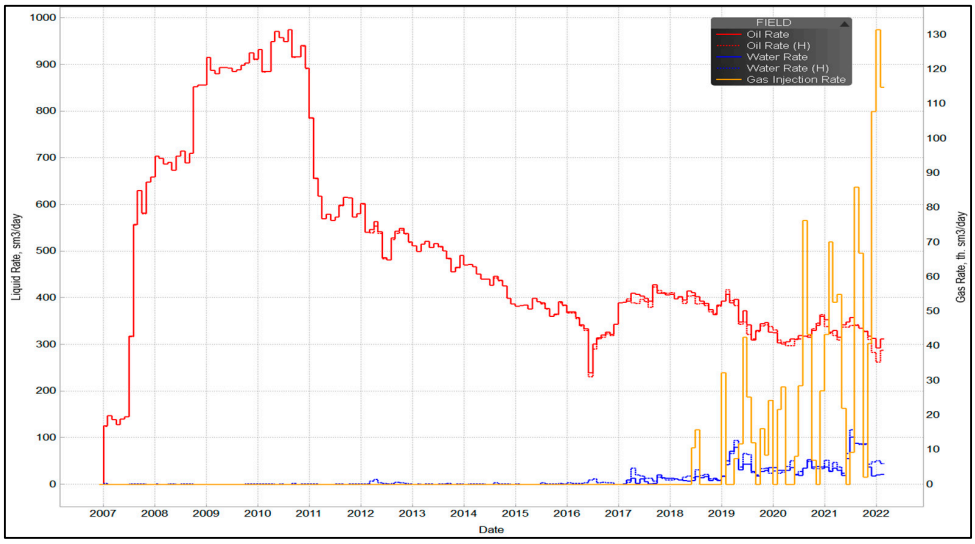


**Figure 6.** Production curves in the intersection region of the S99 unit at different development stages.

### 3.2. Streamline Sweep Analysis

For the convenience of investigating the distribution characteristics of remaining oil and the main controlling factors, this study used the streamline sweep analysis method for further analysis.

Figure 7 displays the streamlines at the initial stage of production. It can be observed that the streamlines were concentrated in the southeast high-production wells. The displacement pressure gradient was low at the initial development stage, and the fluid was mainly plane flow. According to the simulation results, swept pores and hydrocarbon volumes were 1060.8 $\times$ $10^4$ $rm^3$ and 847.1 $\times$ $10^4$ $rm^3$, respectively. The fluid's mean flow rate was obtained utilizing streamline simulation. The simulation results show that the mean and the cumulative plane flow rates were 2.6 $rm^3/d$ and 8.2 $\times$ $10^4$ $rm^3/d$, while the mean and the cumulative vertical flow rates were 2.6 $rm^3/d$ and 8.2 $\times$ $10^4$ $rm^3/d$, respectively.

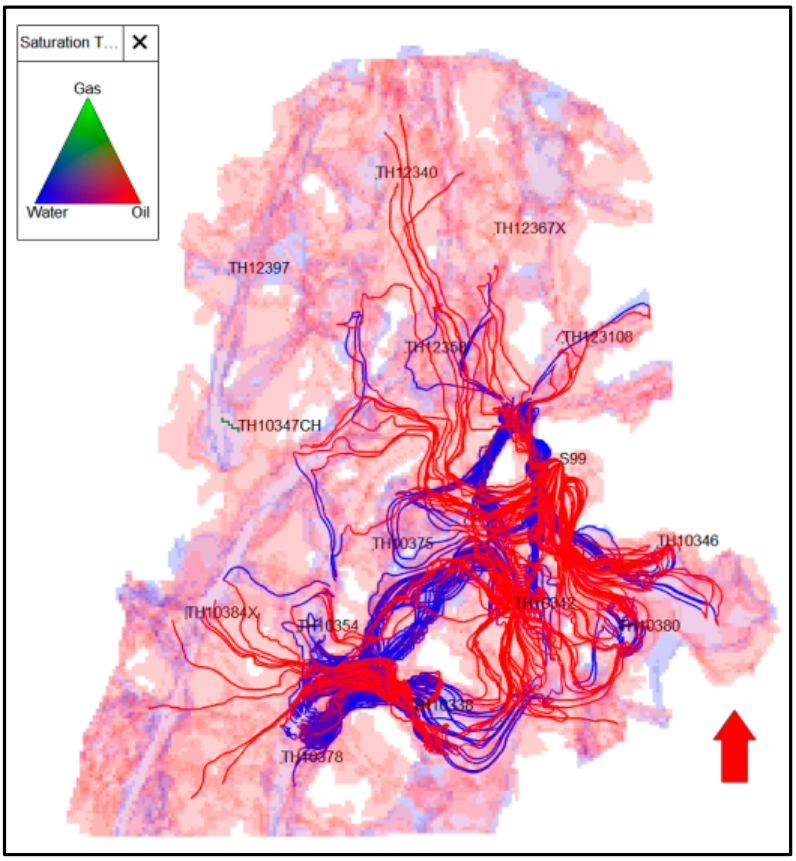


**Figure 7.** Streamline patterns at the initial stage of production.

Figure 8 displays the streamlines at the peak production stage. The streamlines were extensively distributed, and the reservoirs had a wide utilization range. At the peak production stage, various oil wells featured high-liquid exploitation characteristics. This can be attributed to increasing liquid and oil production under an increasing displacement pressure gradient. As a result, the fluid flow process in both plane and vertical directions can be strengthened to varying degrees. Based on the simulation results, the swept range in the reservoir can be obtained. At the peak production, swept pores and hydrocarbon volumes were 1316.2 $\times$ $10^4$ $rm^3$ and 966.7 $\times$ $10^4$ $rm^3$, respectively. In addition, the mean flow velocity of fluid was obtained via streamline simulation. At the peak production stage, the mean and the cumulative plane flow rates were 3.9 $rm^3/d$ and 12.3 $\times$ $10^4$ $rm^3/d$, and the mean and the cumulative vertical flow rates were 2.4 $rm^3/d$ and 7.6 $\times$ $10^4$ $rm^3/d$, respectively.

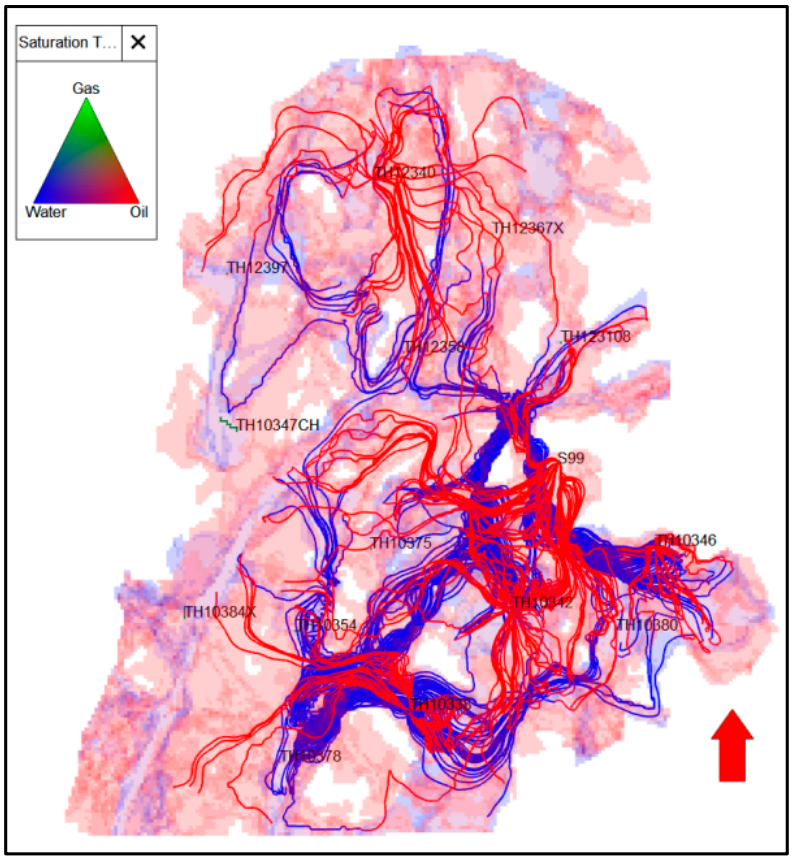


**Figure 8.** Streamline patterns at the peak production stage.

Figure 9 displays the streamlines at the liquid control and oil stabilization stage. In contrast with the condition at the peak production phase, the reservoir's utilization range of remaining oil was expanded in the liquid control and oil stabilization stage, i.e., both single-well range and degree increased. According to actual production data, liquid-control oil production was used, and therefore, the displacement pressure gradient in the reservoir tended to be stable. Through further analysis, at this stage, the fluid flowing process in both plane and vertical directions weakened and tended to be balanced. Based on the present simulation results, the swept range in the reservoir can be obtained. At this stage, swept pores and hydrocarbon volumes were 1088.2 $\times$ $10^4$ $rm^3$ and 757.2 $\times$ $10^4$ $rm^3$, respectively. Meanwhile, the mean flow velocity of fluid can be obtained via streamline simulation. At the liquid control and oil stabilization stage, the mean and the cumulative plane flow rates were 1.5 $rm^3/d$ and 4.7 $\times$ $10^4$ $rm^3/d$, while the mean and the cumulative vertical flow rates were 1.0 $rm^3/d$ and 3.1 $\times$ $10^4$ $rm^3/d$, respectively.

Figure 10 displays the streamlines at the last scale gas injection stage. Compared with the condition at the first three stages, the density of water streamlines dropped obviously, and the density of gas streamlines increased significantly. By simulating the distribution of water content in the reservoir, it was observed that gas injection could cause a certain water coning effect to a certain degree, and water content at the well circumference dropped significantly. In addition, according to the distribution of gas saturation in the reservoir, the injected gas mainly gathered on the top and towards the high-level reservoir bodies along the fractures. As a result, the flow strength of crude oil along the vertical direction dropped. At the last gas injection stage, swept pores and hydrocarbon volumes were 918.3 $\times$ $10^4$ $rm^3$ and 615.6 $\times$ $10^4$ $rm^3$, respectively. The mean flow velocity of fluid can be obtained via streamline simulation. At the liquid control and oil stabilization stage, the mean and the cumulative plane flow rates were 2.4 $rm^3/d$ and 7.4 $\times$ $10^4$ $rm^3/d$, and the mean and the cumulative vertical flow rates were 1.1 $rm^3/d$ and 3.4 $\times$ $10^4$ $rm^3/d$, respectively.

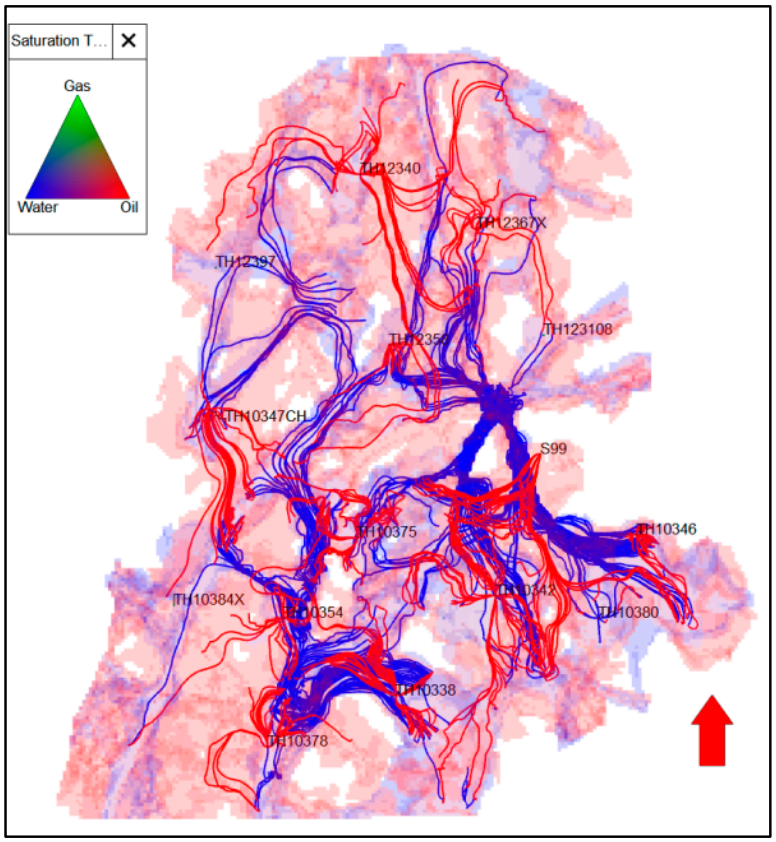


**Figure 9.** Streamline patterns at the liquid control and oil stabilization stage.

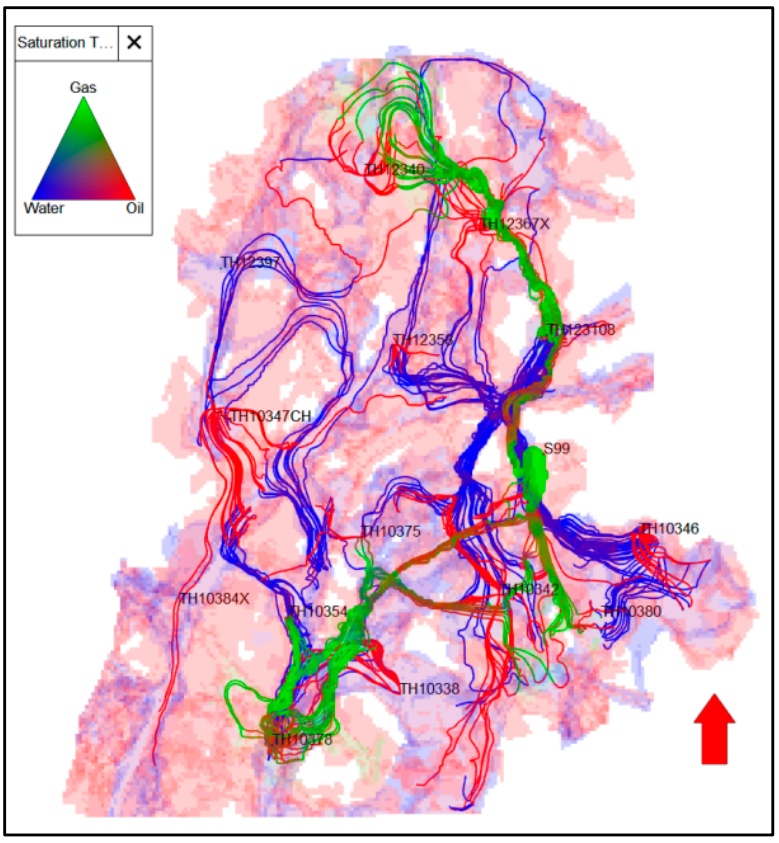


**Figure 10.** Streamline patterns at scale gas injection stage.

### *3.3. Distribution Characteristics of Remaining Oil and Main Controlling Factors*

The distribution patterns of the remaining oil in the reservoirs at different development stages were obtained via simulation. The results are shown in Figure 11. The plane remaining oil was mainly concentrated in the developed regions of southeast caves (TH10338, TH10342, and TH10346) and high-level regions of the northern part of the field (TH12358 and TH12340).

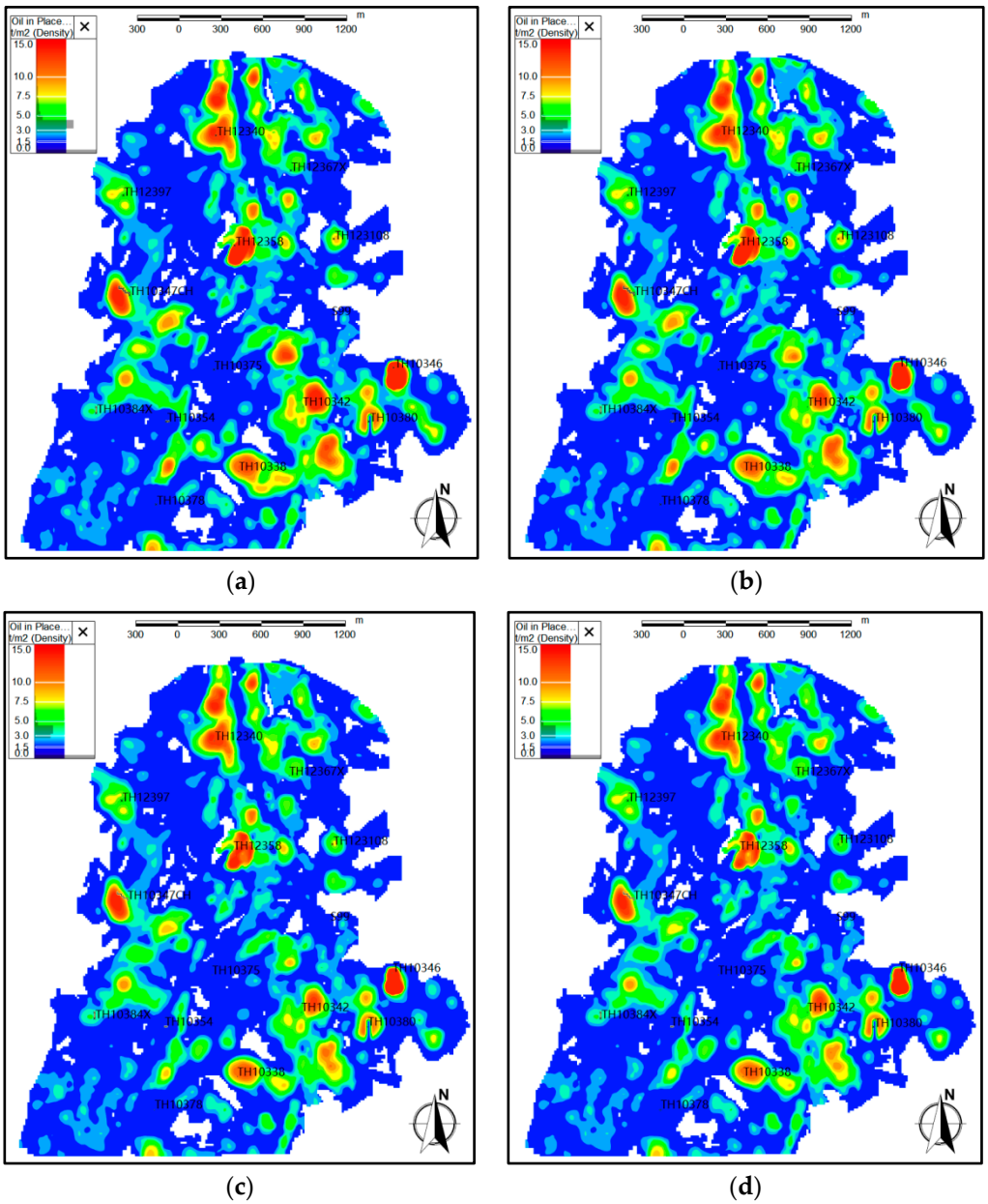


**Figure 11.** Abundance graph of remaining reserves at different development phases. (**a**) At the initial stage of production (December 2007); (**b**) At the peak production stage (December 2010); (**c**) At the liquid control and oil stabilization stage (December 2017); (**d**) At the scale gas injection phase (March 2022).

At the initial stage of development, the reservoir bodies in the intersection region of the S99 unit showed strong connectivity, and the reservoir had a uniform oil-water interface. Initially, the oil-containing thickness was mainly subjected to construction, and the remaining oil accumulated in the ridge-uplifting belt, as shown in Figure 12. With the gradual deepening of the development degree, the oil-containing thickness in the reservoir dropped gradually,

and the mean value dropped was initially 106 m to currently 82 m. Additionally, oil-containing thickness in the southern high-production wells dropped most significantly.

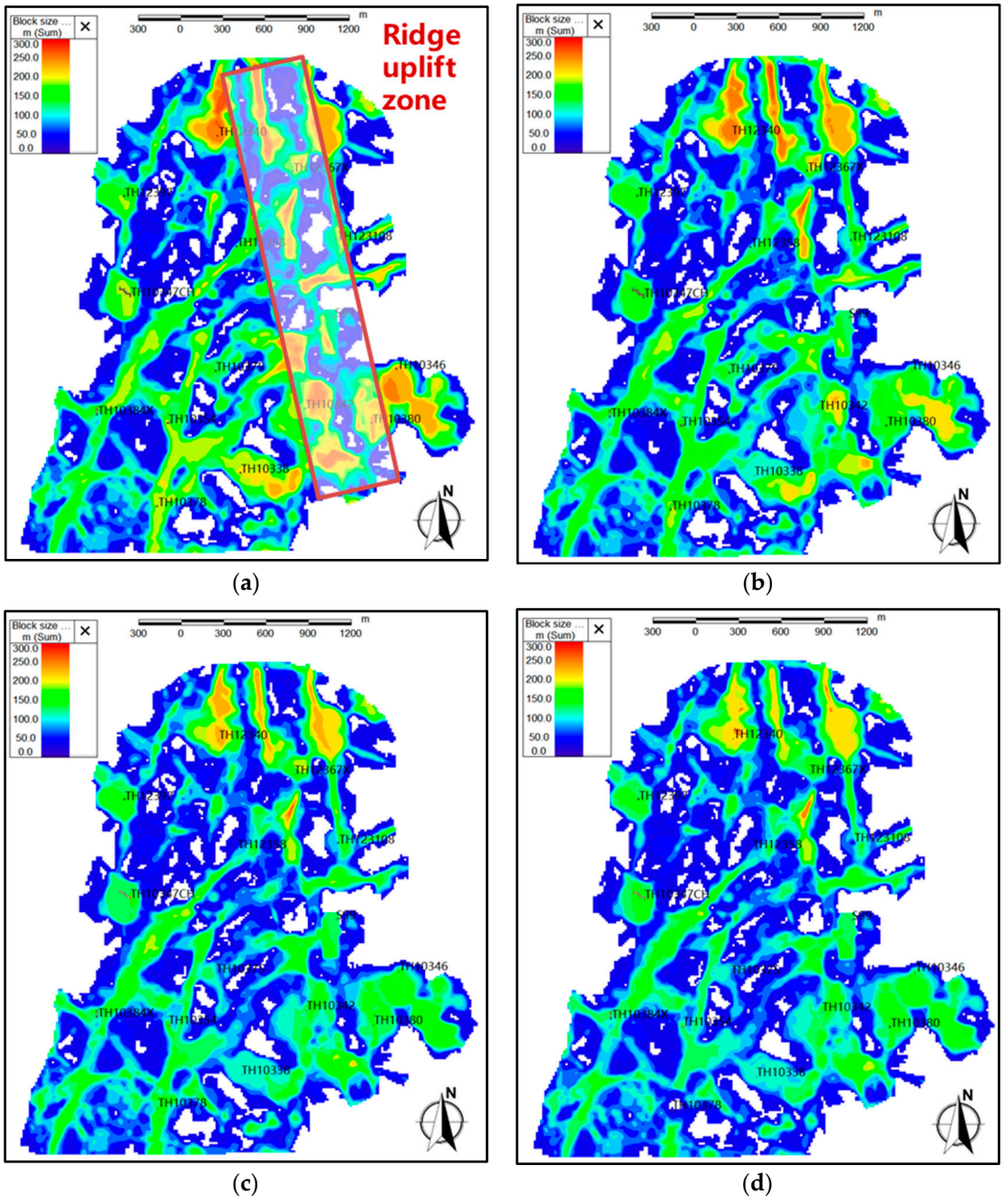


**Figure 12.** Variation of oil-containing thickness at different development stages. (**a**) At the initial stage of production (December 2007); (**b**) At the peak production stage (December 2010); (**c**) At the liquid control and oil stabilization stage (December 2017); (**d**) At the scale gas injection phase (March 2022).

Figure 13 displays the variation of the oil-water interface position in the reservoir and further shows the distribution of longitudinal remaining oil in the reservoir. An obvious bottom water coning problem occurs at the peak production stage. In the late stage, by adopting liquid control and oil stabilization and scale gas injection, the front edge of the water cone became gentle, and water breakthrough risk was effectively controlled. Currently, in terms of longitudinal distribution of remaining oil, the top remaining oil played a dominant role, followed by remaining oil in the unswept region of bottom water. As a result, the mean oil-water interface rose significantly by 24 m from 6250 m to 6226 m.

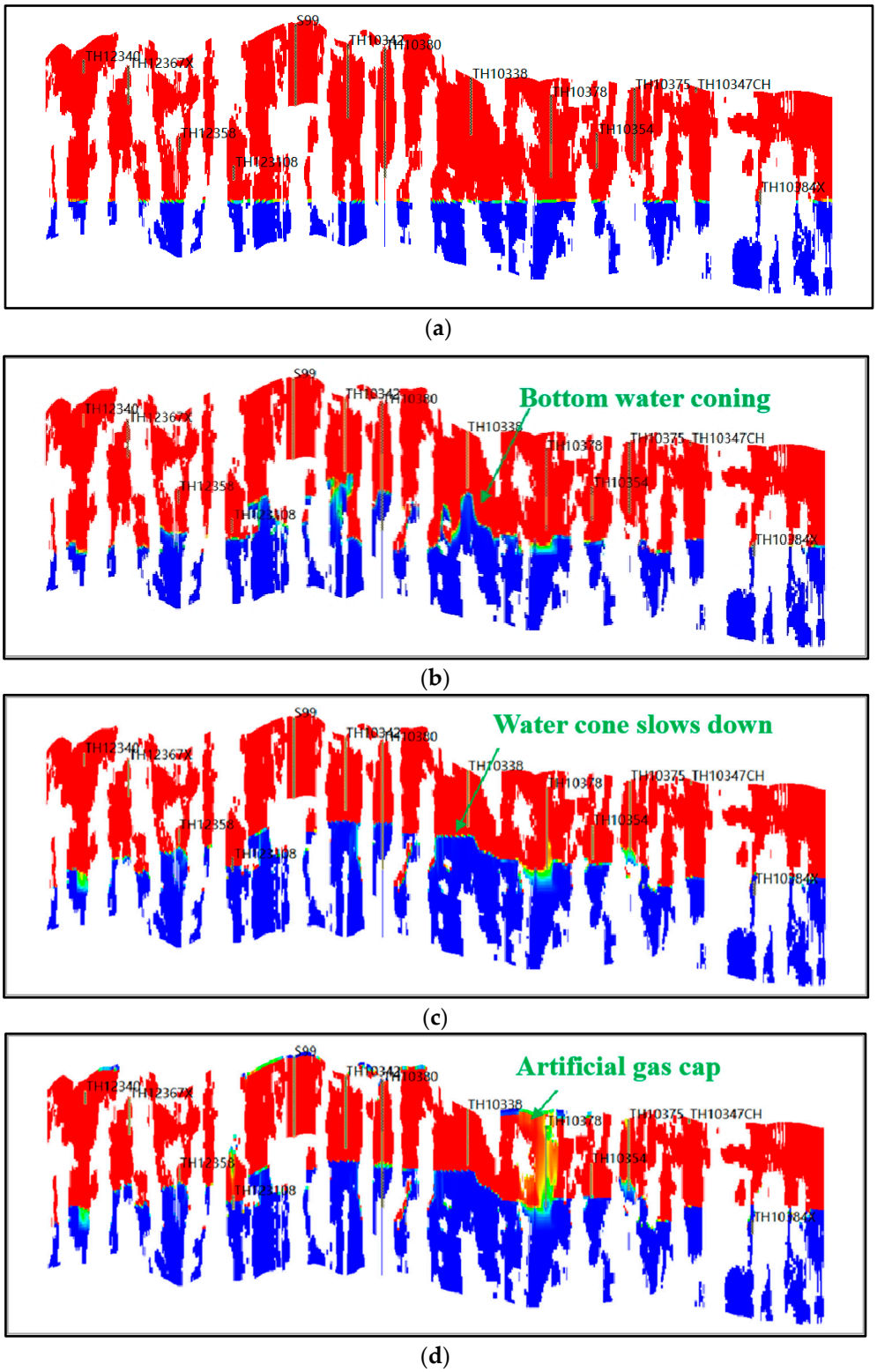


**Figure 13.** Positions of oil-water interfaces at different development stages. (**a**) Mean oil-water interface at the initial stage of production (at 6250 m); (**b**) Mean oil-water interface at the peak production stage (at 6239 m)—Bottom water coning; (**c**) Mean oil-water interface at liquid control and oil stabilization stage (at 6230 m)—Slowing of water coning; (**d**) Mean oil-water interface at scale gas injection stage (at 6226 m)—Artificial gas cap.

Through comprehensive analysis, the main controlling factors of the remaining oil distribution lie in three aspects: (1) Top accumulative remaining oil dominated the high-

level remaining oil in uplifted zones. (2) The remaining oil accumulated in the developed karst cave region. (3) The fracture zones were located at low levels of the two wings of the uplifted zones, and the remaining oil was accumulated in the developed region of fractures.

## 4. Water Invasion Rules and Pattern Analysis

### *4.1. Analysis of Water Invasion Rules*

Bottom water invasion is a central problem during the development of fractured-vuggy reservoirs. Therefore, to examine bottom water invasion and water invasion characteristics during the development of the S99 unit, the geological reserves were meshed to form single-well reserve zones, as shown in Figure 14.

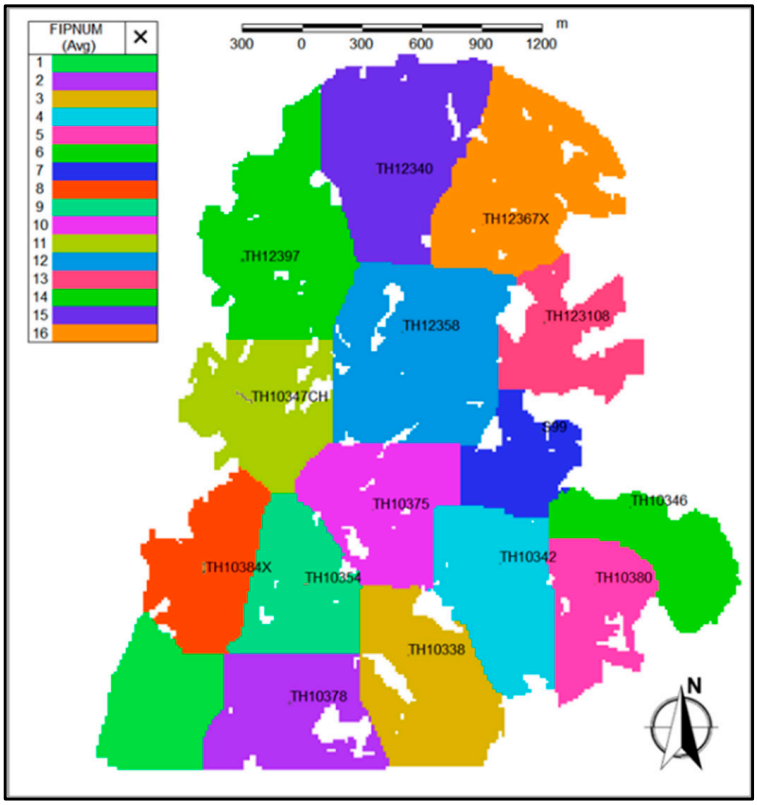


**Figure 14.** Division of single-well zones.

This study also employed quantitative wave and analysis methods based on streamlines to investigate water invasion. The core idea is to calculate the contribution of the injection well and reservoir to the production well with the streamline simulation and simultaneously to determine the bottom water coning direction and source with sink-source analysis on single wells. The calculation principle of the swept volume using the streamline simulation is similar to the injection of the tracer agent into the reservoir during the actual reservoir production process. The swept volume of the injection fluid was calculated based on the characteristics of the production of tracer agent from the production well, including time and concentration. The time of flight of fluid in the reservoir along the streamline was calculated as follows:

$$\tau(x, y, z) = \int \frac{\phi}{|\vec{u}|} ds \quad (1)$$

where $\tau(x, y, z)$ denotes the time of flight of fluid, with a unit of $t$; $\phi$ is a fraction and denotes the porosity; $\vec{u}$ denotes the Darcy velocity, with a unit of m/s; $s$ denotes the flowing distance, m.

In addition, to address the unreliable inter-well connection problem, this study proposed the meshed processing method of geological reserves, i.e., the single-well reserves

were partitioned, and the simulated change of reserves with material balance and compared with the replenishment capacity outside the region. Specifically, the unit reserves were meshed and the fracture-vug relation was engraved in detail. Each mesh controlled a reserve so that the geological reserves equal the sum of all meshed reserves. The replenishment capacity of each mesh was simulated. The data were comprehensively analyzed with the geological model, dynamic data, and streamline analysis to take quantitative interwell flow analysis.

The fluid exchange between the single-well reserves partitions of the S99 well was calculated with the streamline-based quantitative wave and analysis method and interwell flow quantitative analysis method. Results show that TH10375, TH10346, TH12308, TH10342, and TH12358 were the main replenishment zones for fluid in the S99 well-control area, with a replenishment capacity of 11,000, 38,000, 49,000, 93,000, and 132,000 tons, respectively. Accordingly, the proportions of the fluid replenishment capacity of the surrounding wells of the S99 well to the well-control region were calculated, as shown in Figure 15. Overall, the water from the southern region served as the driving source of the S99 well, which passed through the TH10375 zone for external replenishment.

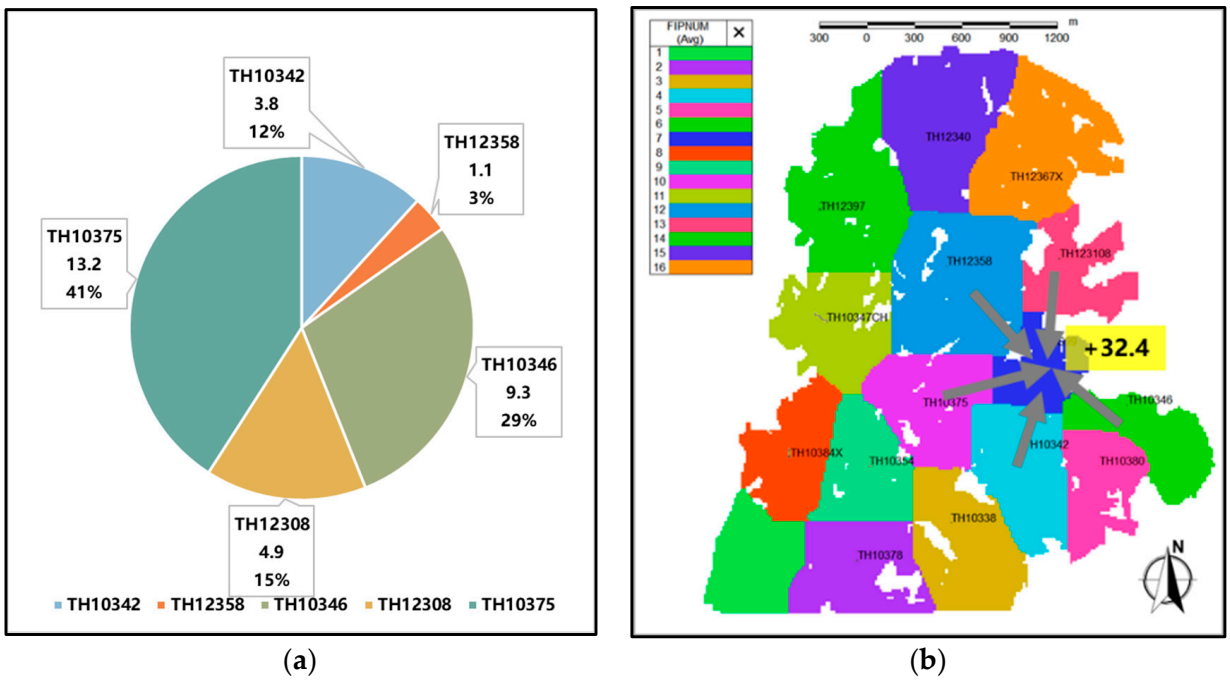


(**a**) (**b**)

**Figure 15.** Illustration of the interwell replenishment of the S99 well ((**a**)Pie chart of S99 outside area replenishment, (**b**) Well control reserves diagram).

The replenishment routes of inter-well flow were correlated with the distributions of water catchment points and fractures. Figure 16 displays the quantitative analysis results of flow behaviors among various wells. The wells with positive replenishment from the outside include S99, TH10342, TH10338, and TH12340 wells, suggesting the replenishment flow from the other regions towards these wells. By contrast, the wells with negative replenishment from the outside are mainly around the water catchment points, including TH10380, TH12397, TH10354, and TH123208, with increased replenishment towards the outside.

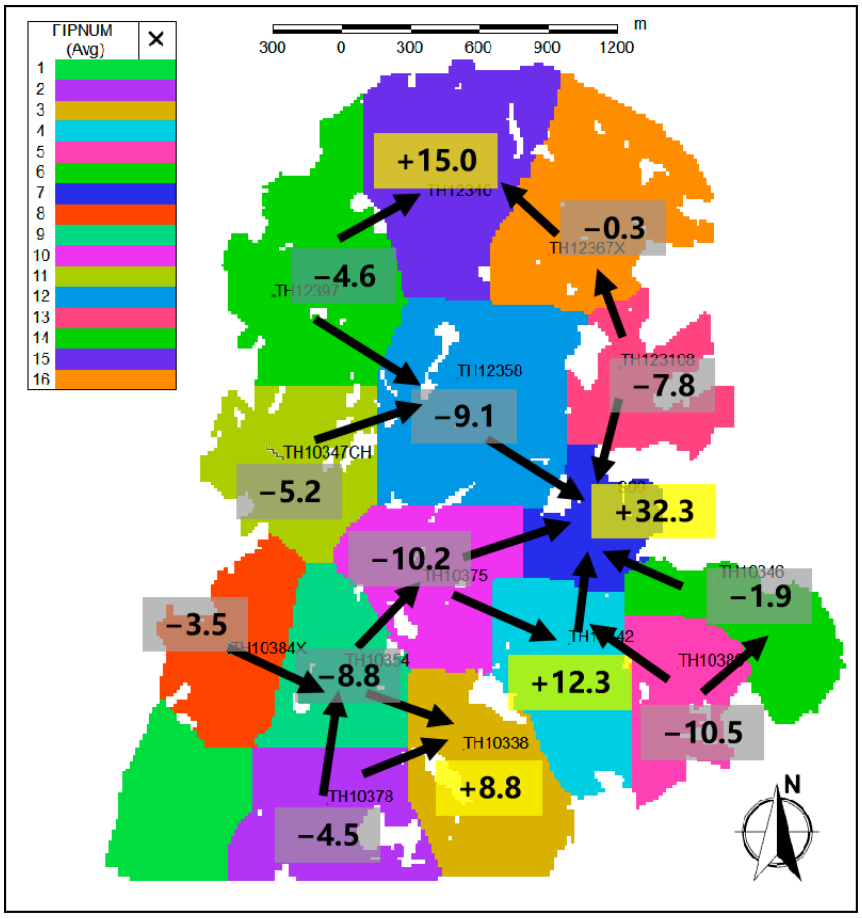


**Figure 16.** Quantitative analysis results of inter-well flow of the S99 unit.

### *4.2. Water Invasion Mode*

The three commonly water-breakthrough modes in the S99 unit are violent flooding, the slow ascension of the water cut, and low water cut or intermittent water production, as shown in Figure 17.

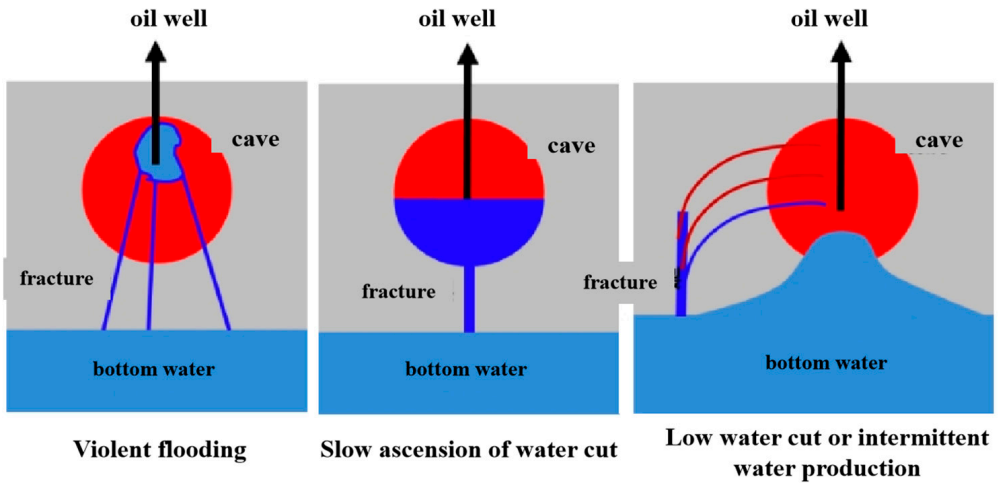


**Figure 17.** Water-breakthrough mode.

Violent flooding is dominated by flow in fractures and bottom rushing along the high-angle fractures. The high-water-content wells in the intersection region of the S99 unit were located in the fracture-developed area with violent flooding mode. Figure 18 displays the streamlines in the typical well TH10380. There existed high-angle fractures at the bottom of the TH10380 well. These fractures were connected, and bottom water directly ran into the TH10380 well via fractures. Accordingly, the streamlines were densely and vertically distributed in the bottom water, suggesting the occurrence of violent water flooding in the TH10380 well.

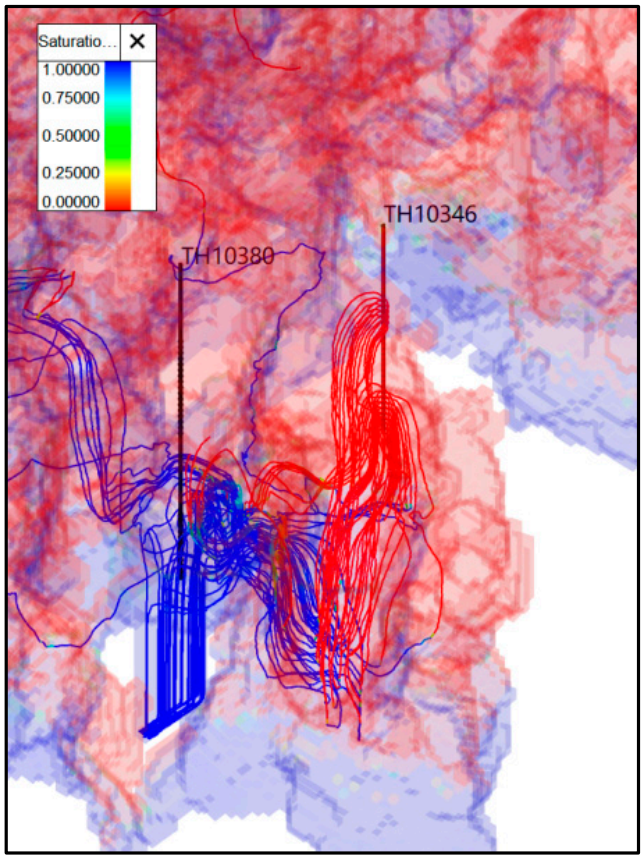


**Figure 18.** Streamlines in the TH10380 well.

Slow ascension of the water cut consists of the slow rising of the water cut and refers to the gradual uplift of the oil-water interface in the solution caverns due to the connection between fractures and bottom water on the bottom. The TH12348 well has a slow ascension mode, as shown in Figure 19. It can be observed from oil-containing saturation curves in well-control regions of TH12348 that the solution caverns showed low filling degrees, affecting water breakthrough rules and the rising velocity of the water cut. It can also be observed from the production curves of the TH12358 well that water cut increased slowly.

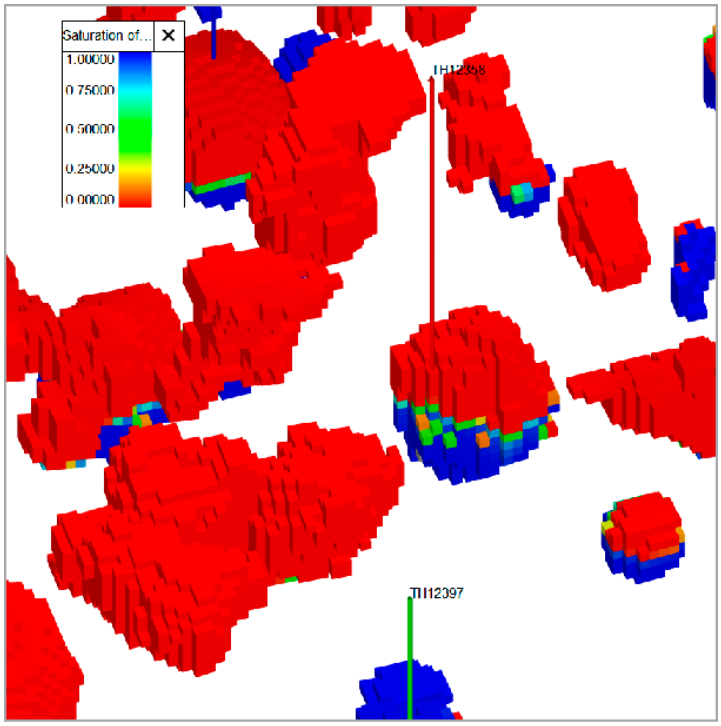


(**a**)

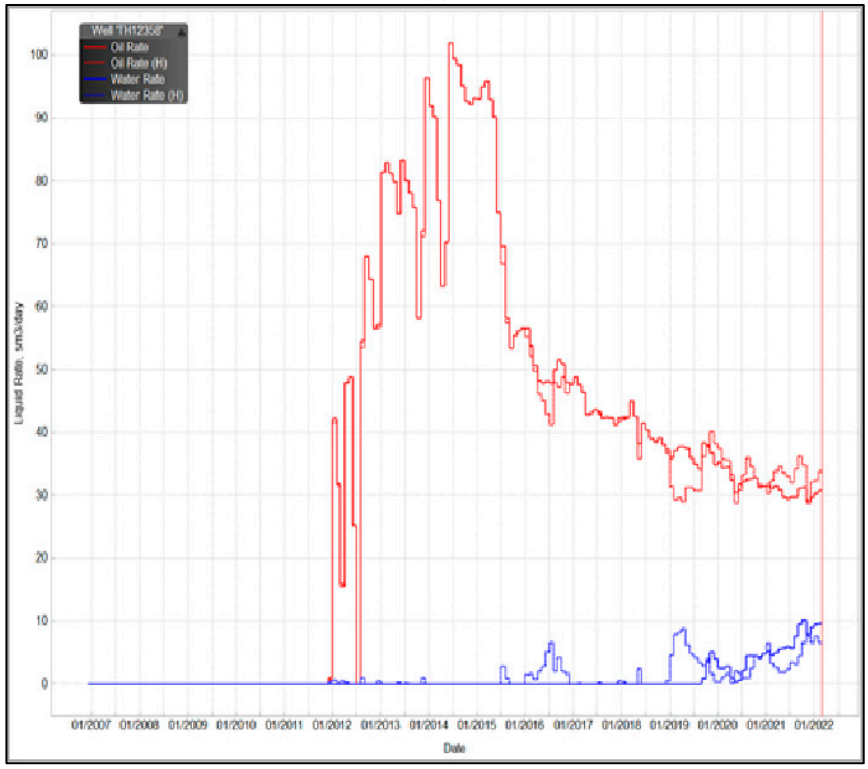


(**b**)

**Figure 19.** Oil-containing saturation (**a**) and production curves (**b**) of the TH12358 well.

Low water cut or intermittent water features flow in solution caverns not directly connected with the vertical fractures and prominent water cones with horizontal flow among fractures. The typical well with this water breakthrough mode is the TH10338 well. According to actual production data, the water content of the TH10338 well was only 3%. Figure 20 shows the bottom water streamlines, from which it can be observed that

bottom water around the TH10338 well rushed along the surrounding faults. Therefore, the bottom water streamlines were densely attributed around the fractures. Afterwards, under the plane displacement pressure difference, the uplifting bottom water migrated to the TH10338 well.

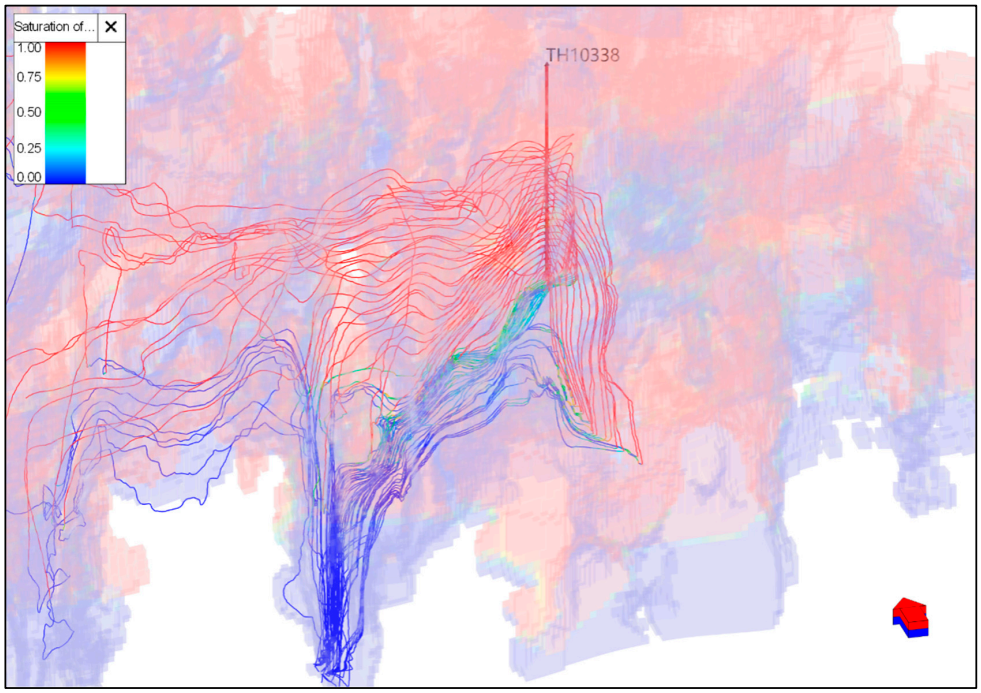


(**a**)

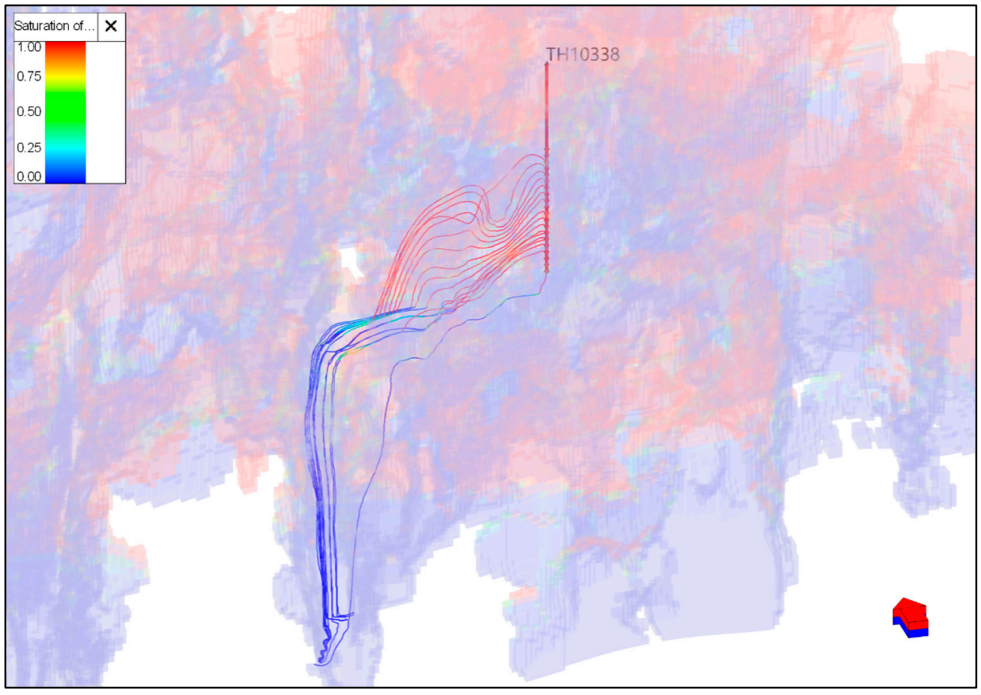


(**b**)

**Figure 20.** Streamline the model of the TH10338 well. (**a**) At the peak production phase; (**b**) At the current phase.

## 5. Conclusions

This study focused on the reservoirs in the intersection region of the S99 unit. Using numerical simulations, the utilization rules, the distribution characteristics of the remaining oil in the fractured-vuggy reservoirs, and water invasion rules and modes were investigated in depth. The main conclusions are described below.

(1) Based on the geological data of the reservoir in the intersection region, the seismic weight was sampled to the geological model with the phase model. Using the same location condition assignment algorithm, four single-type models are fused into a multi-scale discrete three-dimensional geological model of fractured and cavernous reservoirs, and the corresponding fractured-vuggy reservoir model was established for numerical simulation. Various reservoir porosity and permeability conditions were corrected according to the developed static and dynamic data. Moreover, historical fitting was performed on the model, with a single-well fitting precision of over 85%.

(2) The development process can be divided into four stages—the initial stage of production, the peak production stage, the liquid control and oil stabilization stage, and finally, the scale gas injection stage. The utilization condition of remaining oil in the reservoir was examined in combination with the streamline swept analysis method. At the initial production stage, plane flow dominated the fluid flow, and the plane's remaining oil was mainly utilized. At the peak production stage, plane and vertical flow were enhanced, and the remaining oil was used highly efficiently. At the liquid control and oil stabilization stage, both plane flow and the vertical flow weakened, accompanied by a decline in the utilization efficiency of the remaining oil. Finally, water invasion was improved at the scale gas injection stage, and the remaining oil on the top could be utilized.

(3) The remaining oil was mainly distributed in the southeastern vug-developed regions and the northern high-level region. At the initial stage, the oil-containing thickness was mainly subjected to the geologic structure effect, and the remaining oil gathered around the ridge uplifting belt. The remaining oil was mainly on the top in the longitudinal direction and in the region unswept by bottom water. As the development proceeded, the mean oil-water interface was raised by 24 m. Construction, solution caverns, and fractures are the three main controlling factors affecting the remaining oil distribution.

(4) Using the streamline-based quantitative sweep analysis method and inter-well flow quantitative analysis method, flow interchanges among single-well reserve partitions in the S99 well were calculated. Based on source-sink results, the production sources of various wells and the interwell flow relations were quantitatively analyzed. Conclusively, three water breakthrough modes existed: violent flooding, slow ascending of water cut, and low water cut or intermittent water production.

**Author Contributions:** H.C.: Conceptualization, Supervision, Investigation, Writing—review & editing. F.Y.: Investigation, Formal analysis, Writing—original draft, Supervision. S.Z.: Methodology, Investigation. L.L.: Investigation, Formal analysis. X.L.: Methodology, Investigation. B.C.: Methodology, Investigation. All authors have read and agreed to the published version of the manuscript.

**Funding:** This research was funded by the National Science and Technology Major Project of China (2016ZX05053) and the Science and Technology Department Project of Sinopec China Petroleum (ZDP17003).

**Data Availability Statement:** Data available on request from the authors.

**Conflicts of Interest:** The authors declare that they have no known competing financial interests or personal relationships that could have appeared to influence the work reported in this paper.

## References


1. Yang, L.; Kang, Z.; Xue, Z.; Zheng, S. Theories and practices of carbonate reservoirs development in China. *Pet. Explor. Dev.* **2018**, *45*, 712–722.
2. Nairn, A.; Alsharhan, A. *Sedimentary Basins and Petroleum Geology of the Middle East*; Elsevier: Amsterdam, The Netherlands, 1997.
3. Shiyi, Y.; Qiang, W.; Junshi, L.; Haishui, H. Technology progress and prospects of enhanced oil recovery by gas injection. *Acta Pet. Sin.* **2020**, *41*, 1623.
4. Fangzheng, J. Practice and knowledge of volumetric development of deep fractured-vuggy carbonate reservoirs in Tarim Basin, NW China. *Pet. Explor. Dev.* **2019**, *46*, 576–582.
5. Jing, W.; Huiqing, L.; Zhengfu, N.; Hongling, Z.; Cheng, H. Experiments on water flooding in fractured-vuggy cells in fractured-vuggy reservoirs. *Pet. Explor. Dev.* **2014**, *41*, 74–81.
6. Xinbian, L.; Yan, W.; Debin, Y.; Xiao, W. Characterization of paleo-karst reservoir and faulted karst reservoir in Tahe Oilfield, Tarim Basin, China. *Adv. Geo-Energy Res.* **2020**, *4*, 339–348.
7. Cheng, H.; Yang, M. Research of High Pressure Production Characteristics of Fracture Cavity Reservoirs Using Large Cavity Volume High Pressure Physical Model. *Fresenius Environ. Bull.* **2019**, *28*, 8634–8641.
8. Chunhui, D.; Changhe, Y.; Hong, C.; Feiyu, Y.; Yang, Z. Microgravity Monitoring in Fractured-Vuggy Carbonate Reservoirs. *Geofluids* **2023**, *2023*, 5034948.
9. Jing, W.; Wei, Z.; Huiqing, L.; Fangna, L.; Tuozheng, Z.; Liangbin, D.; Xinling, Y.; Bo, L. Inter-well interferences and their influencing factors during water flooding in fractured-vuggy carbonate reservoirs. *Pet. Explor. Dev.* **2020**, *47*, 1062–1073.
10. Cong, T.; Xiaolong, P.; Yang, L.; Yuanshuai, R.; Xiaobo, L. Optimization of Waterflooding Process for Fault-Controlled Fracture-Cavity Reservoir of Ordovician in Tahe Field, Tarim Basin. *Xinjiang Pet. Geol.* **2014**, *35*, 703–707.
11. Jing, W.; Huiqing, L.; Jing, Z.; Qingbang, M.; Huapu, L.; Lizhen, G.; Zhiqiang, Z.; Chang, L. Experimental investigation on water flooding and continued EOR techniques in buried-hill metamorphic fractured reservoirs. *J. Pet. Sci. Eng.* **2018**, *171*, 529–541.
12. Xin, D.; Qingyu, L.; Peichao, L.; Yuxi, X.; Yue, Z.; Detang, L. A novel pressure and rate transient analysis model for fracture-caved carbonate reservoirs. *J. Pet. Sci. Eng.* **2022**, *208*, 109609.
13. Songqing, Z.; Min, Y.; Zhijiang, K.; Zhongchun, L.; Xibin, L.; Kunyan, L.; Xiaobo, L.; Shiliang, Z. Controlling factors of remaining oil distribution after water flooding and enhanced oil recovery methods for fracture-cavity carbonate reservoirs in Tahe Oilfield. *Pet. Explor. Dev.* **2019**, *46*, 786–795.
14. Jing, W.; Liu, H.; Jie, X.; Zhang, H. Formation mechanism and distribution law of remaining oil in fracture-cavity reservoir. *Pet. Explor. Dev.* **2012**, *39*, 624–629.
15. Aifen, L.; Wanjiang, G.; Shuaishi, F.; Jacqueline, N.; Haojun, X.; Xiaofei, L.; Guoqiang, A.; Shiti, C. Experimental investigation of water flooding characteristics and residual oil distribution in filled attic caves reservoir. *Pet. Sci. Technol.* **2021**, *39*, 972–992.
16. Zhongchun, L.; Jianglong, L.; Chengyuan, L.; Zhongliang, T.; Ming, L. Experimental study on effect of reservoir space types on water cut of wells in karstic-fractured carbonate reservoir. *Acta Pet. Sin.* **2009**, *30*, 271–274.
17. Xiao, Y.; Ziwei, Z.; Tongwen, J.; Zhenzhong, C.; Xingliang, D.; Jianfeng, Z. Dynamic and static combination method for fracture-vug unit division of fractured-vuggy reservoirs. *Arab. J. Sci. Eng.* **2018**, *43*, 2633–2640. [CrossRef]
18. Qu, M.; Hou, J.; Qi, P.; Zhao, F.; Ma, S.; Churchwell, L.; Wang, Q.; Li, H.; Yang, T. Experimental study of fluid behaviors from water and nitrogen floods on a 3-D visual fractured-vuggy model. *J. Pet. Sci. Eng.* **2018**, *166*, 871–879.
19. Xinyu, X.; Qinghua, C.; Yinguo, Z.; Jing, W.; Yang, L.; Zhijiang, K.; Hehua, W.; Lianshun, Q.; Yun, Z. Research progress and prospect of Ordovician carbonate rocks in Tahe oilfield: Karst feature. *J. Pet. Explor. Prod. Technol.* **2021**, *11*, 3889–3902.
20. Bochao, T.; Chunying, G.; Mina, H.; Haitao, L.; Ke, R. Research on the Depletion and Recovery Characteristics of Fault-Karst Reservoirs. *Geofluids* **2022**, *2022*, 1105335.
21. Chao, Z.; Linghui, X.; Pingkeng, W.; Zhaomin, L. A novel system for reducing $CO_2$-crude oil minimum miscibility pressure with $CO_2$-soluble surfactants. *Fuel* **2020**, *281*, 118690.
22. Jing, W.; Xiangsheng, Q.; Huiqing, L.; Min, Y.; Xiaobo, L.; Hongguang, L.; Tuozheng, Z. Mechanisms of remaining oil formation by water flooding and enhanced oil recovery by reversing water injection in fractured-vuggy reservoirs. *Pet. Explor. Dev.* **2022**, *49*, 1110–1125.
23. Zihan, G.; Chao, Z.; Teng, L.; Haitao, W.; Zhaomin, L.; Hongyuan, W. Experimental analysis of the stimulation mechanism of CO2-assisted steam flooding in ultra-heavy oil reservoirs and its significance in carbon sequestration. *Fuel* **2023**, *345*, 128188.
24. Wenyang, S.; Jian, C.; Yongchuan, L.; Min, C.; Lei, T.; Jiajia, B.; Qingjie, Z. Pressure transient analysis of horizontal wells in multibranched fault-karst carbonate reservoirs: Model and application in SHB oilfield. *J. Pet. Sci. Eng.* **2023**, *220*, 111167.
25. Ming, Y.; Xiaobo, L.; TAO, T.; Qing, L.; Hongguang, L.; Yixiao, Z. Remaining oil distribution and potential tapping measures for palaeo-subterranean river reservoirs:A case study of TK440 well area in Tahe Oilfield. Reserv. *Eval. Dev.* **2020**, *10*, 43–48.
26. Hai, T.; Juan, H.; Yuansuai, R.; Xiaobo, L. Study on water drive law and characteristics of remaining oil distribution of typical fault-karst in faultkarst reservoirs, Tahe Oilfield. *Editor. Dep. Pet. Geol. Recovery Effic.* **2018**, *25*, 95–100.
27. Lihu, C.; Jinsheng, S.; Bo, Z.; Nu, L.; Yuqiang, X. Sensitivity analysis of the temperature profile changing law in the production string of a high-pressure high-temperature gas well considering the coupling relation among the gas flow friction, gas properties, temperature, and pressure. *Front. Phys.* **2022**, *10*, 1112.
28. Yueliang, L.; Zhenhua, R.; Tao, Y.; Dindoruk, B. Using propanol as an additive to $CO_2$ for improving $CO_2$ utilization and storage in oil reservoirs. *Appl. Energy* **2022**, *311*, 118640.

29. Peng, C.; Shaoying, C.; Yongjin, Z.; Jinlong, S.; Zhangfeng, Q.; Guanming, S.; Xiaowei, S. New method for characterizing internal structure of fault-karst reservoirs and analysis on acidizing fracturing effect: A case study in HLHT oilfield, Tarim Basin, NW China. *Lithosphere* **2021**, *2021*, 6784641.
30. Wei, H.; Yaping, Y.; Chanjuan, X. Cobalt-Catalyzed Reductive Carboxylation of Aryl Bromides with Carbon Dioxide. *Greenh. Gases Sci. Technol.* **2019**, *9*, 965–978.
31. Ping, Y.; Zhiwei, X.; Haohan, L.; Xiaofan, C.; Zhongliang, G. Application of water injection curves for the dynamic analysis of fractured-vuggy carbonate reservoirs. *J. Pet. Sci. Eng.* **2018**, *169*, 220–229.
32. Peiliang, L.; Lin, J.; Bochao, T.; Ke, R.; Mina, H.; Chunying, G. Residual Oil Distribution Pattern in a Fault-Solution Carbonate Reservoir and Countermeasures to Improve Oil Development Effectiveness. *Geofluids* **2022**, *2022*, 2147200.
33. Shouya, W.; Zhaomin, L.; Zhuangzhuang, W.; Hemanta, K.S.; Chao, Z.; Mingxuan, W. Investigation of $CO_2/N_2$ injection in tight oil reservoirs with confinement effect. *Energy Sci. Eng.* **2020**, *8*, 1194–1208.
34. Haoran, Z.; Yun, L.; Chuanxian, L.; Bo, Y.; Fei, Y.; Shuangshuang, L.; Haoping, P.; Pengfei, Y. Experimental and mechanism investigation on flowability and wax deposition of waxy crude oil with dissolved CH4 by pressurized laboratory apparatus. *Fuel* **2023**, *343*, 127907.
35. Zhengxiao, X.; Zhaomin, L.; Zhiliang, L.; Binfei, L.; Qifeng, Z.; Lei, Z.; Yongjin, S.; Maen, M.H. Characteristics of $CO_2$ foam plugging and migration: Implications for geological carbon storage and utilization in fractured reservoirs. *Sep. Purif. Technol.* **2022**, *294*, 121190.
36. Liu, Y.; Rui, Z. A storage-driven $CO_2$ EOR for a net-zero emission target. *Engineering* **2022**, *18*, 79–87. [CrossRef]
37. Hanlie, C.; Lianshan, W.; Jianmin, W. Characteristics of water breakthrough in ordovician fractured vuggy type reservoirs in thr eastern tazhong area. *J. Chongqing Univ. Sci. Technol. (Nat. Sci. Ed.)* **2016**, *18*, 45–48.
38. Chao, Z.; Pingkeng, W.; Zhaomin, L.; Tao, L.; Ling, Z.; Dongdong, H. Ethanol enhanced anionic surfactant solubility in $CO_2$ and $CO_2$ foam stability: MD simulation and experimental investigations. *Fuel* **2020**, *267*, 117162.
39. Shouya, W.; Zhaomin, L.; Chao, Z.; Guangzhong, L.; Peng, Z. Nanohydrodynamic Model and Transport Mechanisms of Tight Oil Confined in Nanopores Considering Liquid–Solid Molecular Interaction Effect. *Ind. Eng. Chem. Res.* **2021**, *60*, 18154–18165.
40. Fangfang, C.; Xinguo, D.; Yuchun, Y. charateristics of exploration and development of fractured-vuggy carbonate rock oil poor in Tarim oilfield of China. *J. Chengdu Univ. Technol. (Sci. Technol. Ed.)* **2012**, *39*, 606–610.
41. Wu, S.; Li, Z.; Sarma, H.K. Influence of confinement effect on recovery mechanisms of $CO_2$-enhanced tight-oil recovery process considering critical properties shift, capillarity and adsorption. *Fuel* **2020**, *262*, 116569. [CrossRef]
42. Baohua, C.; Wei, X.; Shusheng, G. Variation rule of water cut in large-scale fractured-cavernous reservoir. *Pet. Geol. Recovery Effic.* **2011**, *18*, 80–82+86.
43. Soleimani, M. Well performance optimization for gas lift operation in a heterogeneous reservoir by fine zonation and different well type integration. *J. Nat. Gas Sci. Eng.* **2017**, *40*, 277–287. [CrossRef]
44. Soleimani, M.; Mining, F.O. Petroleum and Geophysics. Naturally fractured hydrocarbon reservoir simulation by elastic fracture modeling. *Pet. Sci.* **2017**, *14*, 286–301. [CrossRef]